

# Cubic ferromagnet and its emergent phenomenon in the vicinity of phase boundary

Wei-Lin Tu,<sup>1,\*</sup> Xinliang Lyu,<sup>2</sup> S. R. Ghazanfari,<sup>2</sup> Huan-Kuang Wu,<sup>3</sup> Hyun-Yong Lee,<sup>1,4,5,†</sup> and Naoki Kawashima<sup>2,6,‡</sup>

<sup>1</sup>*Division of Display and Semiconductor Physics, Korea University, Sejong 30019, Korea*

<sup>2</sup>*Institute for Solid State Physics, University of Tokyo, Kashiwa, Chiba 277-8581, Japan*

<sup>3</sup>*Department of Physics, Condensed Matter Theory Center and Joint Quantum Institute, University of Maryland, College Park, MD 20742, USA*

<sup>4</sup>*Department of Applied Physics, Graduate School, Korea University, Sejong 30019, Korea*

<sup>5</sup>*Interdisciplinary Program in E-ICT-Culture-Sports Convergence, Korea University, Sejong 30019, Korea*

<sup>6</sup>*Trans-scale Quantum Science Institute, The University of Tokyo, Bunkyo, Tokyo 113-0033, Japan*

(Dated: September 13, 2022)

Among the natural materials displaying magnetism, it is well-known that the magnetic anisotropy can be widely found and it affects the fundamental physics. However, the technical difficulty have been keeping the problem out of reach for a long time. In this work, we study the simplest lattice spin model for the two-dimensional (2D) cubic ferromagnet by means of mean-field analysis and tensor network calculation. While both methods give rise to similar results in detecting related phases, the 2D infinite projected entangled-pair state (iPEPS) calculation provides more accurate values of transition points. Moreover, our iPEPS results indicate that it is more difficult in pinning down the direction of magnetic easy axes near the phase boundary, and we interpret it as the easy-axis softening. By constructing a low-energy effective model in the reduced Hilbert basis, an emergence of  $U(1)$  symmetry is diagnosed which explains the softening of easy axes. We argue that, from the perspective of field theory and renormalization group, the emergence of continuous symmetry becomes exact right on the critical points and the criticality is governed by the 3D XY universality class. Numerical correlation functions obtained by iPEPS also support this physical scenario. Our study, to the best of our knowledge, provides the very first systematic analysis upon this lattice spin model beyond the mean-field consideration. We also address the practical importance of such emergent phenomenon and its possible application in manipulating the magnetic easy axes for spinful semiconductors.

## I. INTRODUCTION

Magnetic materials are highly crucial to the civilization with a long history. When the temperature drops below the Curie point, spins as the microscopic objects amount to a collective behavior and ferromagnetism forms. In the most general picture, where spins enjoy the unitary transformation in three dimensions, formation of magnetic order stands for the breaking of  $O(3)$  symmetry group. However, due to many possible reasons such as the lattice structure, within real-world materials the ferromagnetic moment tends to align along certain directions, the so-called easy axes. When the easy-axis orientation follows the principal or diagonal direction of the cubic (isometric) crystal structure, they are referred to as the cubic ferromagnets [1, 2]. In fact, no matter being weak or strong it is a very common feature for the magnetic materials and thus affects the microscopic mechanism. Unlike the picture of spontaneously breaking a continuous symmetry, however, its true nature is less known due to the difficulty of probing this issue.

Recently, layered magnetic materials have drawn researchers' attention because of its broad range of potential applications within the two-dimensional (2D) layers [3]. Among them, the ferromagnetic semiconductor thin film is of special interest because of its promising features from industrial point of view [4], and various magnetic anisotropies can also be

found in these materials [5]. In many related works upon such magnetic materials, the determination of easy-axis alignment plays an important role in their studies, in order to explain the experimental observation. However, the introduction of quantum entanglement and its possible influence in the low temperature are seldom discussed because most studies follow the mean-field paradigm. Moreover, despite a great amount of effort for its theoretical understanding through Zener's or other phenomenological models [5], the microscopic picture is often overlooked.

In order to describe the behavior of spin in a lattice, a model composed of an isotropic short-range superexchange coupling with a single-ion term, which breaks the  $O(n)$  symmetry, was first proposed by Sinha *et al.* in explaining the phase transition of uranium arsenide [6]. It has later been shown by Sznajd and Domański that the Landau free energy of this many-body Hamiltonian leads to the corresponding Landau-Ginzburg-Wilson (LGW) Hamiltonian being the  $n$ -vector model with a cubic anisotropy [7, 8]. This simplest lattice model with cubic anisotropy is free from the vicious sign problem, but still remains hard to probe with quantum Monte Carlo (QMC) due to an unexpected freezing of local spin moments, an issue that we will address in Appendix A. To the best of our knowledge, there has been no elaborated result beyond the mean-field studies [7–11] so far for this model, despite some more recent studies showing the possible existence of quadrupolar phase with easy axes aligning along  $\langle 100 \rangle$  in one dimension by utilizing the perturbation theory and density-matrix renormalization group (DMRG) [12–14].

Due to the growing interest in investigating the 2D ferromagnets with cubic anisotropy, it is very desirable to study this many-body Hamiltonian with an appropriate numerical tool,

\* weilintu@korea.ac.kr

† hyunyoung@korea.ac.kr

‡ kawashima@issp.u-tokyo.ac.jp

aiming to provide a more profound understanding of its physical scenario. For such purpose, we adopt the 2D tensor network ansatz in the thermodynamic limit, the infinite projected entangled-pair states (iPEPS) [15–17], in order to take into account the quantum entanglement among sites which goes beyond the mean-field treatment for uncovering its more precise phase diagram. As we will show in the following content, near the phase boundary our numerical results suffer from an unexpected local-minimum issue which is absent deep inside the canted phase. According to the argument from the perturbative renormalization group (RG), the appearance of local minima underlines an emergent symmetry taking place right at the critical points. Since the lattice model that we study here is highly related to real-world materials [6], this phenomenon might imply a great potential upon (1) making 2D cubic ferromagnets a good platform in studying the behavior of emergent symmetry and (2) practical usage in magnetic thin films, about which we will discuss in the following content.

## II. LATTICE MODEL WITH CUBIC ANISOTROPY

### A. Hamiltonian

As mentioned in the Introduction, in this work we are interested in the cubic ferromagnetic thin films and its simplest many-body Hamiltonian in the square lattice is [10]

$$H = -J \sum_{\langle i,j \rangle} \vec{S}_i \cdot \vec{S}_j + K \sum_{i,\alpha} (S_i^\alpha)^4 - h \sum_i S_i^z \quad (1)$$

$$= H_J + H_{K-h},$$

with  $S = 2$  and  $\alpha = x, y, z$ . We divide the Hamiltonian into  $H_J$  and  $H_{K-h}$  for later convenience. Spins on nearest-neighbor sites ( $\langle i, j \rangle$ ) are connected through a ferromagnetic Heisenberg interaction ( $J > 0$ ). The second term reflects the cubic anisotropy and with  $K > 0$ , its easy axes go along  $\langle 111 \rangle$ . In this work we assign  $K = 1$  as the energy unit. For a 2D magnet, especially the semiconductor thin film, frequently it functions under an external magnetic field. Thus, a Zeeman term along  $z$ -axis is also considered when a magnetic field is present. Note that Eq. (1) does not commute with the total-spin operator:  $[H, \sum_i S_i^z] \neq 0$ , and thus it does not possess the spin (or particle) conservation symmetry, meaning that the additional phase factor introduced by  $U(1)$  transformation will alter the Hamiltonian. Furthermore, with a non-zero  $h$  that deforms the original cubic lattice into a tetragonal one, we have only four favored directions for the magnetization lying above the  $x - y$  plane. In fact, the symmetry group of our model can be probed by replacing  $(\pm S^\beta, \pm S^{\bar{\beta}})$  with  $\beta, \bar{\beta} = x, y$  and  $\beta \neq \bar{\beta}$  into Eq. (1) while leaving itself unchanged. Such transformation includes 4 rotations and 4 reflections in the plane, and thus they compose a dihedral group with order 4 or written as  $D_8$  in the abstract algebra. By choosing  $K = 1$  in this work, four favored directions possess azimuthal angles  $\theta$ , shown in Fig. 1(a), equal to  $\pi/4, 3\pi/4, 5\pi/4$ , and  $7\pi/4$ . In what follows, we restrict  $\theta$  to be in the range  $\theta \in [0, \frac{\pi}{4}]$  without loss of generality.

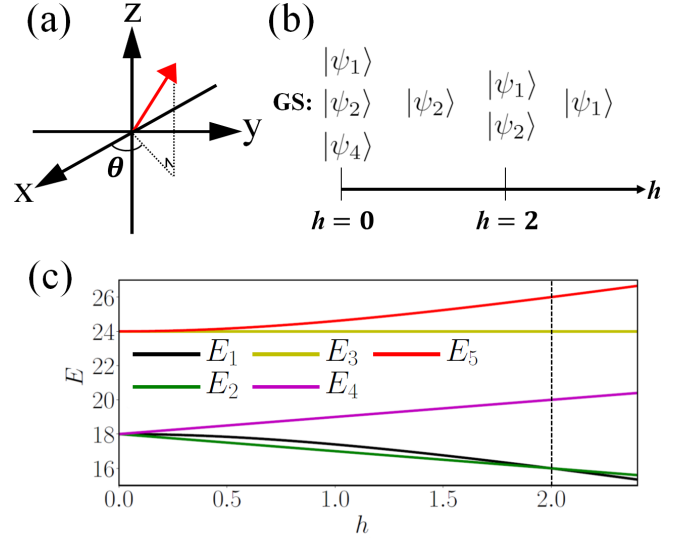


FIG. 1. (a) The spontaneous magnetization (the red arrow) and the angle  $\theta$ . When a canted phase appears, planar magnetic order points in a certain direction with relative angle  $\theta$  to the  $x$ -axis ( $[100]$ ). (b) Ground-state phase diagram for the single-site Hamiltonian ( $J = 0$ ). Definition for each state is recorded in Eq. (2). (c) The eigenenergy for each local state along with  $h$ . Energies are calculated according to Eq. (3) and (4). Dashed line at  $h = 2$  indicates the degenerate (transition) point.

### B. The one-site ( $J = 0$ ) limit

We begin our discussion from studying one special case as  $J$  is chosen to be zero. Under this choice,  $H = H_{K-h}$  and it is a one-site Hamiltonian which can be directly solved. Because  $S = 2$ , the local Hilbert space is five-dimensional and  $S_z = 1, 0$ , and  $-1$  states are still good eigenstates. On the other hand, due to the quartic term  $S_z = 2$  and  $-2$  states are connected and new eigenbasis needs to be formed. The results are

$$\begin{bmatrix} |\psi_1\rangle \\ |\psi_2\rangle \\ |\psi_3\rangle \\ |\psi_4\rangle \\ |\psi_5\rangle \end{bmatrix} = \begin{bmatrix} N(|2\rangle - \alpha|-2\rangle) \\ |1\rangle \\ |0\rangle \\ |-1\rangle \\ N(\alpha|2\rangle + |-2\rangle) \end{bmatrix}, \quad (2)$$

where  $|2\rangle, |1\rangle, |0\rangle, |-1\rangle$ , and  $|-2\rangle$  represent the eigenstates of  $S^z$  with

$$\alpha = \frac{\sqrt{4h^2 + 9} - 2h}{3} (\leq 1), \quad (3)$$

$$N = \frac{1}{\sqrt{\alpha^2 + 1}}.$$

The corresponding eigenvalues are

$$\begin{bmatrix} E_1 \\ E_2 \\ E_3 \\ E_4 \\ E_5 \end{bmatrix} = \begin{bmatrix} -3\alpha^{-1} + 21 + 2h \\ 18 - h \\ 24 \\ 18 + h \\ 3\alpha + 21 + 2h \end{bmatrix}, \quad (4)$$

with  $E_n$  being the eigen-energy of  $|\psi_n\rangle$ . We note that the formation of this “reshuffled” Hilbert basis results from the fact that the  $K$  and  $h$  terms do not commute. Therefore, a new set of orthonormal basis is generated. By varying  $h$ , we plot the ground state (GS) phase diagram in Fig. 1(b). There are two special points where degeneracy takes place. One is at  $h = 0$  with a three-fold degeneracy among  $|\psi_1\rangle$ ,  $|\psi_2\rangle$ , and  $|\psi_4\rangle$ . The other lies at  $h = 2$  with a two-fold degeneracy between  $|\psi_1\rangle$  and  $|\psi_2\rangle$ . We will especially focus on the vicinity of the second degenerate point,  $h = 2$ . There, a transition of the two-level system takes place, meaning that a first-order transition happens with a sudden jump of the order parameter  $\langle S^z \rangle$ , with  $\langle \psi_1 | S^z | \psi_1 \rangle = 1.6$  and  $\langle \psi_2 | S^z | \psi_2 \rangle = 1$  where  $S^z = \frac{1}{N} \sum_i S_i^z$  and  $N$  stands for the number of lattice sites. This two-level transition corresponds to the Ising or the liquid-gas transition and with *a priori* knowledge for the later systems, there is a critical temperature,  $T_c$ , above which  $|\psi_1\rangle$  and  $|\psi_2\rangle$  become indistinguishable and the continuous phase transition at  $T_c$  belongs to the Ising universality class.

We also plot the eigen-energies (Eq. (4)) along  $h$  for each state in Fig. 1(c). One obvious feature lies in the fact that as  $h$  is strong enough,  $|\psi_3\rangle$ ,  $|\psi_4\rangle$ , and  $|\psi_5\rangle$  are largely gapped from the rest two states. Moreover,  $|\psi_1\rangle$  and  $|\psi_2\rangle$  share very close energies around  $h = 2$ . The above observations suggest that near the transition point, other higher-energy states can only serve as the “tie-breaker” through quantum fluctuation after we turn on  $J$ . This will become an important feature in the following discussion.

### C. Inclusion of Heisenberg coupling

We will now study the effect while including the  $J$  term. As mentioned in the previous section, the Heisenberg term serves as the tunneling from low-energy states to higher ones. It will also introduce the inter-site correlation that leads to a collective behavior of local spins, forming the ferromagnetic state. Our remaining task is to investigate all possible phases after  $J$  is turned on and try to probe the critical behavior on the phase boundary.

Initially, we can first try to picture what kinds of phases could emerge. From the information of  $H_{K-h}$ , we have learned that there is a two-level system and both states are gapped. Therefore, they will remain until  $J$  is strong enough to overcome the energy difference between  $|\psi_1\rangle$  and  $|\psi_2\rangle$ , thus triggering a phase transition. Since both of them are polarized in the  $z$ -direction, we call them the polarized states,  $P_1$  and  $P_2$ , coming from  $|\psi_1\rangle$  and  $|\psi_2\rangle$  respectively. Note that although from the symmetry point of view both  $P$  phases are identical, because of the two-level nature we label them with different indices, same as the fact that we call the phase of matter with isotropically translational invariance possessing a larger (smaller) density the liquid (gas) phase. Besides the polarized phase as  $J$  is strong enough the condensation takes place, leading to the off-diagonal magnetic moments. Therefore, we expect that a canted ( $C$ ) phase, whose magnetization no longer aligns along the  $z$ -axis, should also appear in the phase diagram. The transition between  $P$  and  $C$  phases then

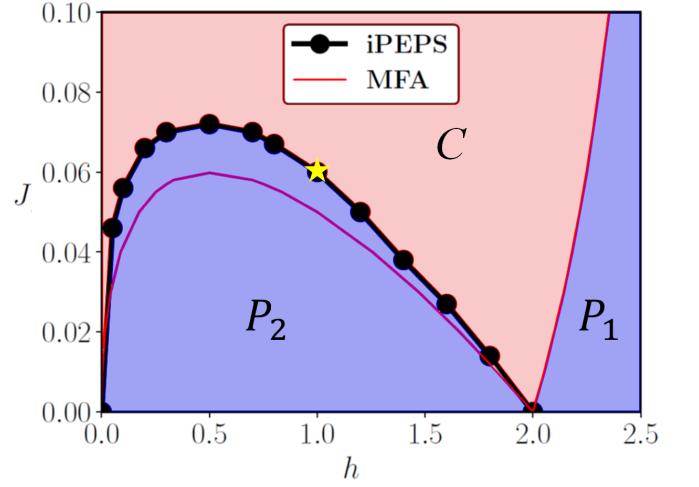


FIG. 2. The phase diagram by MFA (red thin lines) and iPEPS (circle symbols) with  $D = 4$  ( $\chi = 70$ ). For MFA, phase boundaries are obtained by self-consistently solving Eq. (5). Two polarized ( $P_1$  and  $P_2$ ) phases are connected through  $h = 2$  while canted ( $C$ ) phase forms when  $J$  comes into play. The yellow star indicates the transition point probed by iPEPS with  $(D, \chi) = (5, 50)$ . See Section II C 2 and Appendix B 2 for detailed discussion.

becomes the central issue in the following content.

#### 1. Mean-field analysis

We first study the effect of  $J$  with mean-field approximation (MFA), sometimes also referred to as the molecular field approximation. The mean-field Hamiltonian reads

$$H_{\text{MF}} = -J \sum_{\langle i, j \rangle} \vec{S}_i \cdot \langle \vec{S}_j \rangle + \sum_{i, \alpha} (S_i^\alpha)^4 - h \sum_i S_i^z. \quad (5)$$

By introducing the mean-field of  $\langle \vec{S}_j \rangle$  Eq. (5) again reduces to a one-site Hamiltonian and can be solved iteratively by assuming the local state to be

$$|\psi_{\text{local}}\rangle = c_0 |\psi_1\rangle + \sum_{m=1}^4 c_m e^{i\phi_m} |\psi_{m+1}\rangle, \quad (6)$$

where  $c_0 = \sqrt{1 - \sum_m c_m^2}$ . Then, we variationally optimize the parameter set  $\{c_m, \phi_m\}$  in lowering the energy,  $\langle H_{\text{MF}} \rangle$ . To diagnose  $P$  and  $C$  phases, we rely on the order parameter

$$M_p = \sqrt{\langle S^x \rangle^2 + \langle S^y \rangle^2}, \quad (7)$$

where  $M_p$  is nonzero in  $C$  phase [10]. We plot the mean-field phase diagram in Fig. 2 as red thin lines, along with the phase boundary by iPEPS which will be discussed in the later sections. Besides  $M_p$ , another relevant observable is  $M_z = \langle S^z \rangle$ . Recall that at  $J = 0$ , we have a sudden jump of  $M_z$  at  $h = 2$ , indicating the first-order transition. Because of the ferromagnetic nature, we can adopt the translational invariance in our calculation and thus  $\langle S^\alpha \rangle = \langle S_i^\alpha \rangle$ . For the

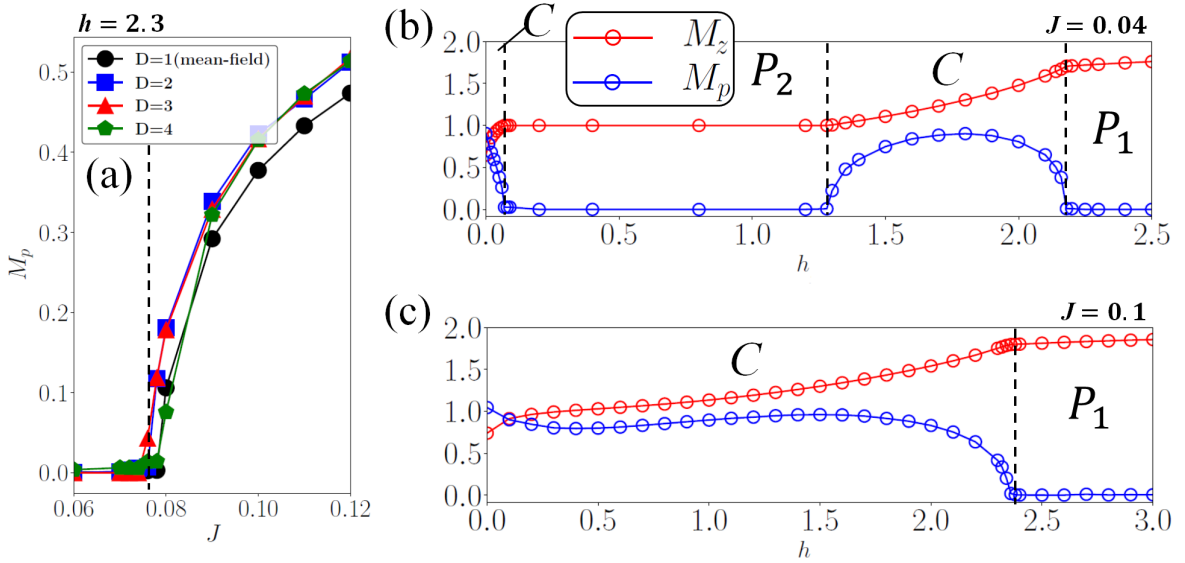


FIG. 3. iPEPS calculations ( $D = 4$  and  $\chi = 20$ ) for (a) The order parameter ( $M_p$ ) probed by different bond dimensions along a vertical cut at  $h = 2.3$ , and the plots of  $M_z$  and  $M_p$  observables along with  $h$  for (b)  $J = 0.04$  and (c)  $J = 0.1$ . A  $C \rightarrow P_2 \rightarrow C \rightarrow P_1$  phase transition can be clearly seen in (b), while only two phases are detected in (c).

$P_2$  phase  $M_z \simeq 1$  while  $M_z > 1.6$  for the  $P_1$  phase beyond  $h = 2$  (cf.  $\langle \psi_1 | S^z | \psi_1 \rangle = 1.6$  and  $\langle \psi_2 | S^z | \psi_2 \rangle = 1$  at  $h = 2$ ). Notice that  $M_z$  does not have to be strictly equal to 1 because it is not a good quantum number.

We emphasize two points here: (1)  $M_z$  is not an order parameter because in all phases it is non-zero. And (2) when  $h = 0$  the cubic symmetry is restored with 8 preferable directions of magnetization. In fact, it can be sensed from Eq. (2) and (4) that when  $h = 0$ , we have a three-fold degeneracy among  $|1\rangle$ ,  $|-1\rangle$ , and  $|\psi_1\rangle$  which is equal to  $\frac{1}{\sqrt{2}}(|2\rangle - |-2\rangle)$ . In our study we focus on the scenario when  $h \neq 0$ ; therefore, inside the  $C$  phase  $M_p$  always favors one of the tetragonal directions, which is consistent with previous results [10].

If we take a look at the optimized parameter set,  $\{c_m, \phi_m\}$ , we can see that the coefficient of a higher-energy  $|\psi_m\rangle$  is proportional to  $J/(E_m - E_g)$ , where  $E_m$  is its corresponding eigen-energy and  $E_g$  is the ground state energy at  $J = 0$ :  $E_g = E_1$  ( $E_2$ ) at  $h > 2$  ( $< 2$ ). Therefore, we can learn from Fig. 1(c) that as  $J$  remains relatively small, the coefficients of  $|\psi_1\rangle$  and  $|\psi_2\rangle$  should be dominant. Moreover, the phase factors,  $\phi_1$  to  $\phi_4$ , provide extra degrees of freedom in lowering  $\langle H_{MF} \rangle$ . According to our MFA, in  $C$  phase  $(\phi_1, \phi_2, \phi_3, \phi_4) = (5\pi/4, 3\pi/2, 7\pi/4, 0)$ , suggesting that a coherence is attained and it leads to the  $\theta = \pi/4$  magnetization. It is crucial to note that such coherence is a consequence of our reshuffled local Hilbert space because in the sole Heisenberg ferromagnets there is no easy axis after the spontaneous symmetry breaking.

By far the physical scenario we have found agrees quite well with our intuitive assumption. The next question is if we can exploit a better numerical tool in order to provide a more accurate phase diagram.

## 2. iPEPS study

With a frustration-free many-body spin Hamiltonian, QMC is usually the prior option for conducting numerical studies. However, due to the difficulty that we elucidate in Appendix A, it is unlikely to numerically solve Eq. (1) by applying QMC. Therefore, we need to seek for another numerical tool and iPEPS will be applied for our purpose. The technical details of this tensor network ansatz and its detection of the phase transition points will be discussed in the Appendix B, and we only focus on the results here.

The black circles in Fig. 2 pin down the estimated transition points by iPEPS with bond dimensions  $(D, \chi) = (4, 70)$ . To strengthen the reliability, we also provide one point probed with  $(D, \chi) = (5, 50)$ , which is the upper limit of our machine's capacity, in yellow star symbol. The estimated transition point is equal to the one of  $D = 4$  within a small  $J$  variance ( $\Delta J = 0.002$ ). Thus, we believe that the phase boundary present here is already very close to that of  $D \rightarrow \infty$ .

As we can clearly see, the phase boundary of  $P_2$  dome is quantitatively different from the one by MFA, suggesting an improvement after adopting iPEPS. For the other boundary at  $h > 2$ , on the other hand, MFA is already very accurate. In Fig. 3(a) we present the order parameter,  $M_p$ , obtained with different bond dimensions using iPEPS along the  $h = 2.3$  vertical cut. All the different trials predict a transition point at around  $J = 0.076$  (dashed line), meaning that the iPEPS calculation with  $D > 1$  does not provide a better prediction. It is not surprising because the second boundary serves as the saturation line, beyond which the product state of  $|\psi_1\rangle$  is a well estimated ansatz for its GS even with a nonzero  $J$ .

In Fig. 3(b) and (c), we demonstrate two horizontal cuts of relevant observables,  $M_z$  and  $M_p$ , for  $J = 0.04$  and  $J = 0.1$ . As shown in Fig. 3(b),  $M_p$  is nonzero in the beginning for

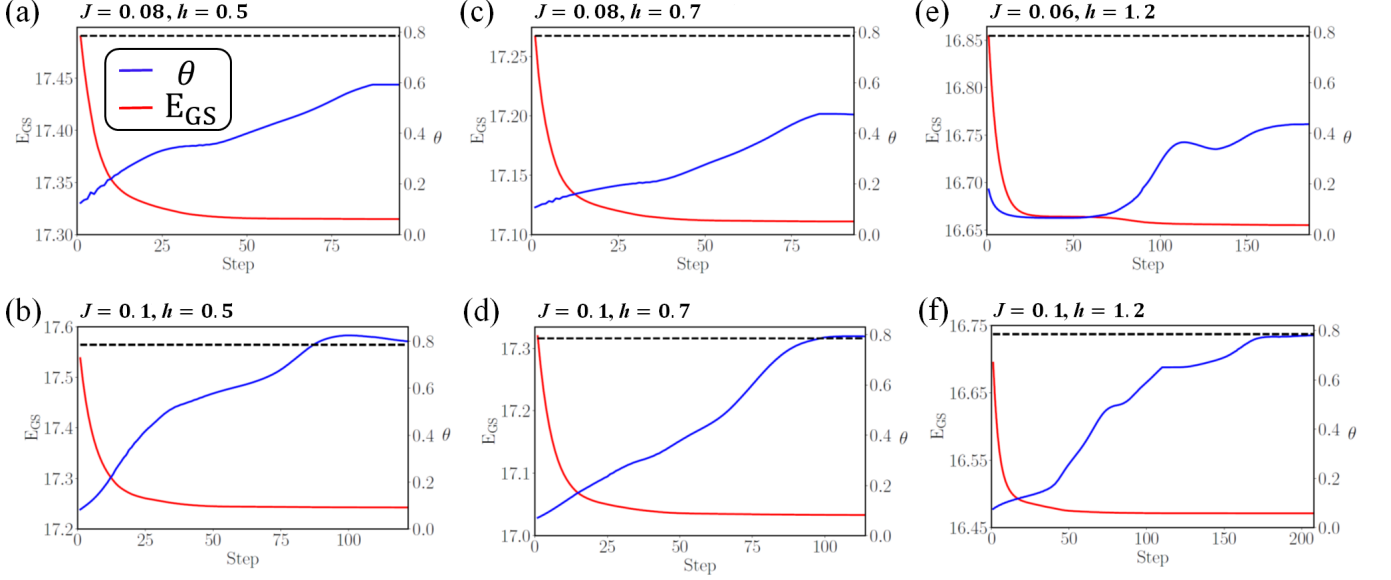


FIG. 4. Plots of ground state energy ( $E_{GS}$ ) and azimuthal angle ( $\theta$ ) defined in Fig. 1(a) during the optimization process with  $D = 4$  for points near ((a), (c), and (e)) and away from ((b), (d), and (f)) the  $P_2$  dome. The issue of local minimum is manifest in the upper row while not for the trials in the lower row.

	$E_{GS}$	$\theta_c/\pi$	$M_z$	$M_p$
$(J, h) = (0.08, 0.5)$	17.31491	0.18845	1.00833	0.64239
	17.31426	0.25130	1.00884	0.62537
$(J, h) = (0.08, 0.7)$	17.11102	0.15063	1.03210	0.70821
	17.11022	0.24194	1.03301	0.68585
$(J, h) = (0.06, 1.2)$	16.65518	0.00018	1.08426	0.74180
	16.65518	0.04029	1.08427	0.74277
	16.65529	0.09014	1.08398	0.74496
	16.65527	0.12205	1.08426	0.74618
	16.65528	0.13893	1.08433	0.74967
	16.65509	0.19642	1.08440	0.73746
	16.65513	0.22317	1.08450	0.74337
	16.65509	0.25318	1.08475	0.73936

TABLE I. We provide the detailed numbers of simulations for three points near the  $P_2$  dome. Numbers for trials with and without the local-minimum issue are shown in the first and last rows for each point with  $D = 4$  and  $\chi = 20$ . The energy difference among distinct ansatz for  $(J, h) = (0.06, 1.2)$  is especially less apparent, whose reason will be explained in Section III A.

small  $h$  and then becomes zero entering the  $P_2$  phase dome. As the magnetic field is further enhanced,  $M_p$  appears again in  $C$  phase. Finally, the state gets saturated and  $M_p$  disappears. Such phase transition corresponds to the re-entrant  $C \rightarrow P_2 \rightarrow C \rightarrow P_1$  transition revealed in Ref. [10]. When  $J$  is large enough outside the  $P_2$  phase dome, however, we end up with only one  $C$  and  $P_1$  phases, as demonstrated in Fig. 3(c) for  $J = 0.1$ .

However, a peculiar phenomenon happens as we approach the  $P_2$  phase dome. We have discovered that the more our calculation suffers from the local-minimum issue. In Fig. 4 we have sam-

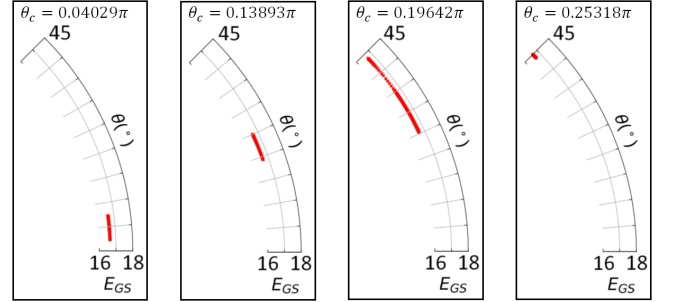


FIG. 5.  $\theta$ - $E_{GS}$  profiles for four distinct trials in Table I of  $(J, h) = (0.06, 1.2)$  are demonstrated. During the optimization process, as the intermediate  $E_{GS}$  is smaller than the threshold value 16.656, the corresponding  $\theta$  and energy are indicated with red dots in the one-eighth pie chart.

pled several points near ((a), (c), and (e)) and away from ((b), (d), and (f)) the phase boundary and plotted the variation of GS energy ( $E_{GS}$ ) and  $\theta$  during the optimization process, all starting from the same random initial input. As we can see, while at those points away from the phase boundary each trial converges to a canted ferromagnetic state with the converging angle  $\theta_c \approx \pi/4$ , close to the boundary the convergence flows to some local minima. For a better comparison, in Table I we provide the detailed values of  $E_{GS}$ ,  $\theta_c$ , and physical observables for the simulations of the points near the boundary. For  $h = 0.5$  and  $0.7$  we demonstrate two distinct results: values in the local and (nearly) global minima. The globally minimal results are generated through the optimization starting from a converged ansatz nearby, which gives rise to a  $\theta = \pi/4$  magnetic easy axis. It is clear to see that despite some energy

differences,  $\Delta E$  is smaller than 0.005% of  $E_{\text{GS}}$ . From the values of  $M_z$  and  $M_p$  we also realize that it is not simply the numerical artifacts when getting too close to the phase boundary, because  $M_p$  is quite apparent and even larger than the 0.6 times of  $M_z$ .

For  $h = 1.2$ , where the local-minimum issue is even more manifest, more data are shown with different directions of easy axis. While the energy difference among them is even smaller than 0.0015% of  $E_{\text{GS}}$ , an ansatz giving rise to magnetic easy axis along the principal axis ( $\theta_c/\pi = 0.00018$ ) can also be detected. For a better demonstration, in Fig. 5 we exhibit the  $\theta$  of ansatz during the optimization process when the final convergence is well approached for several trials in Table I. From the values of  $E_{\text{GS}}$  in the table, converging ansatz all give energies smaller than 16.656. As a result, we set this number as the threshold and plot the  $\theta$  of ansatz when its energy already drops below 16.656 during the optimization process. From Fig. 5 we can see that despite a larger or smaller fluctuation of  $\theta$  near the final convergence, different trials flow to different  $\theta_c$  which suggests the issue of emerging local minima. Overall, we see that the whole  $E_{\text{GS}} < 16.656$  profile almost cover all the  $\theta \in [0, \pi/4]$  region. We interpret the above observation from our numerical results as the “softening” of easy axis, because as we get closer to the phase boundary among ansatz giving different  $\theta_c$  they possess nearly indistinguishable energy difference.

In fact, the appearance of local minima is a common issue for iPEPS calculation, especially when the energy gradient is very small near the global minimum of Hilbert space manifold, or it is near the phase boundaries of first-order transition. Since the latter scenario of a discontinuous transition does not apply here, it is reasonable to deduce that near the phase boundary the convergence toward the globally minimal point becomes more difficult with the gradient decent algorithm. This implies an unexpected emergent phenomenon near the transition points.

### III. DISCUSSION

#### A. Low-energy effective theory

To unveil the cause of this local-minimum issue, let us first try to gain more understanding from the perspective of the lattice model by proposing an effective theory. From Fig. 1(c) we can clearly see that there is a large energy gap that separates  $|\psi_1\rangle$  and  $|\psi_2\rangle$  from the rest states. Therefore, when  $J$  is enough to overcome the rather small energy difference between  $E_{\psi_1}$  and  $E_{\psi_2}$ , a phase transition can be triggered. In the vicinity of phase boundary (or inside the  $P_1$  and  $P_2$  phases), we can project out the rest states other than  $|\psi_1\rangle$  and  $|\psi_2\rangle$  on each site

$$\begin{aligned} H^{\text{eff}} &= PHP \\ &= P(-J \sum_{\langle i,j \rangle} \vec{S}_i \cdot \vec{S}_j)P + \sum_{i,n} E_n |\psi_n^i\rangle \langle \psi_n^i| \\ &= H_J^{\text{eff}} + H_{K-h}^{\text{eff}}, \end{aligned} \quad (8)$$

where  $P = \Pi_i (1 - \sum_{m=3}^5 |\psi_m^i\rangle \langle \psi_m^i|)$  is the projection operator and  $n = 1, 2$ . Because we have the following relations

$$\begin{aligned} \langle \psi_1 | S^z | \psi_1 \rangle &= 2N^2(1 - \alpha^2), \\ \langle \psi_2 | S^z | \psi_2 \rangle &= 1, \\ \langle \psi_1 | S^+ | \psi_2 \rangle &= \langle \psi_2 | S^- | \psi_1 \rangle = 2N, \end{aligned} \quad (9)$$

while all the other terms are zero, the first term becomes

$$H_J^{\text{eff}} = -J \sum_{\langle i,j \rangle} \vec{\tau}_i \cdot \vec{\tau}_j, \quad (10)$$

with

$$\tau^+ = (\tau^-)^\dagger = \begin{bmatrix} 0 & 2N \\ 0 & 0 \end{bmatrix}, \tau^z = \begin{bmatrix} 2N^2(1 - \alpha^2) & 0 \\ 0 & 1 \end{bmatrix}. \quad (11)$$

With further elaboration, Eq. (10) can be expressed as

$$H_J^{\text{eff}} = -t_J \sum_{\langle i,j \rangle} (\sigma_i^+ \sigma_j^- + \sigma_i^- \sigma_j^+) + V_J \sum_{\langle i,j \rangle} \sigma_i^z \sigma_j^z - B_J \sum_i \sigma_i^z, \quad (12)$$

where  $t_J = 2JN^2$ ,  $V_J = -J\gamma_1^2$ , and  $B_J = 4J\gamma_1\gamma_2$  with  $\gamma_1 = N^2(1 - \alpha^2) - \frac{1}{2}$  and  $\gamma_2 = N^2(1 - \alpha^2) + \frac{1}{2}$ ;  $\sigma$  stands for the Pauli matrices (see Appendix C).  $H_J^{\text{eff}}$  represents a hard-core bosonic (HCB) Hamiltonian with an attractive potential under a magnetic field.

Since effectively  $H_{K-h}^{\text{eff}}$  is equivalent to an auxiliary “field” that discriminates  $|\psi_1\rangle$  and  $|\psi_2\rangle$  (telling us where we are close to the first or second phase boundary), near the vicinity of phase boundary the properties of  $C$  phase can be well described by  $H_J^{\text{eff}}$ . Through the direct evaluation we learn that  $|t| \gg |V|$  for the parameters of interest here; therefore a superfluid condensation is favorable. More importantly, Eq. (12) has a global  $U(1)$  symmetry, meaning that after the spontaneous symmetry breaking its free energy does not change by an acquisition of an extra phase factor ( $e^{i\phi}$ ) to the order parameter. This explains the reason why we suffer from the local-minimum issue near the phase boundary during the numerical simulation.

The above-mentioned scenario becomes exact only when we can completely ignore the effect from  $|\psi_3\rangle$  to  $|\psi_5\rangle$ , suggesting that a sufficiently large energy gap is required and the tunneling ( $J$ ) should be small ( $\lesssim |E_1 - E_2|$ ). This is the reason why we still observe the  $\theta = \pi/4$  canted state deep inside the  $C$  phase, because there  $J$  is much larger than  $|E_1 - E_2|$  and thus higher-energy states come into the play, fixing the magnetic easy axes along the tetragonal directions. Moreover, as  $h$  is small the energy gap also decreases (Fig. 1(c)); therefore the picture described by Eq. (12) loses some credibility and the emergent phenomenon is less manifest, which also adheres to our observation to the numbers shown in Table I. In sum, both our numerical results and theoretical analysis point out a feasibly emergent phenomenon near the phase boundary and we interpret it as the emergence of  $U(1)$  symmetry.

## B. Field theory interpretation

### 1. Classical field theory

In the previous section we have unveiled the fact that the  $U(1)$  symmetry which does not originate from our model gradually emerges approaching the phase boundary. We then need to check whether it becomes exact right on the critical points. This is feasible because there the correlation length diverges and thus those higher-energy terms causing the anisotropy, which we neglect in Eq. (8), become truly irrelevant [18–20]. To see whether it is true, we will extend the previous discussion by means of the field theory. The critical behavior of  $O(n)$  model with cubic anisotropy has been extensively studied through the momentum-space renormalization group (RG) [21–23], the Wilson’s legacy, for a LGW Hamiltonian composed of the  $n$ -vector model plus a diagonal quartic field term [24, 25]. Such LGW Hamiltonian possesses the following form [25]

$$\mathcal{H} = \int d^d x \left\{ \frac{1}{2} [(\nabla \phi)^2 + r \phi^2] + u \phi^4 + v \sum_{i=1}^n (\phi_i)^4 \right\}, \quad (13)$$

where  $(\nabla \phi)^2 = \sum_{i=1}^n (\nabla \phi_i)^2$  and  $\phi^2 = \sum_{i=1}^n (\phi_i)^2$ .  $d$  stands for the real-space dimension and  $n$  reflects the component of field  $\phi$ . As the standard measure for a field Hamiltonian up to the quartic field terms, the physics as  $d < 4$  should be treated in a perturbative way with the  $\epsilon = 4 - d$  expansion [26] in order to pin down the fixed point for the critical behavior. The leading-order RG flow is shown in Appendix D.

While the physical scenario does not change with higher-order  $\epsilon$ -expansion, the value of critical component,  $n_c$ , will be altered when a further calculation is conducted. To date, the most reliable results from  $\epsilon$ -expansion studies up to six-loop calculation [27, 28], Monte Carlo [29], and a very recent bootstrapping method [30] all indicate  $2.85 < n_c(d = 3) < 3$ , suggesting that the Heisenberg cubic ferromagnet ( $n = 3$ ) in three dimensions should undergo a cubic phase transition when the temperature is dropping down to its Curie point. An important message from the RG prediction also tells us that when  $n < n_c$ , the transition is governed by a continuous symmetry which the original Hamiltonian does not possess, meaning that the anisotropy term becomes irrelevant right at the transition point. This fact signifies an emergence of continuous symmetry on the phase boundary. Indeed, a number of previous works have suggested such possibility by studying the antiferromagnetic transverse-field frustrated Ising model (TFFIM) in (2+1) dimensions with LGW approach or Monte Carlo simulation [31–33].

Since Eq. (1) contains a Zeeman term, we need to reconsider its effective LGW Hamiltonian in the field theory. For our phase transition of interest,  $P \rightarrow C$ , the corresponding order parameter is  $M_p = \sqrt{M_x^2 + M_y^2}$ , where  $M_\alpha = \langle S^\alpha \rangle$  and  $\alpha = x, y$ . Therefore we can write down its corresponding free energy up to the fourth power [10]

$$\mathcal{F} = \mathcal{F}_0 + \frac{r}{2} M_p^2 + u M_p^4 + v (M_x^4 + M_y^4), \quad (14)$$

where  $\mathcal{F}_0 = \mathcal{F}_0(M_z, h)$ . We ignore the higher-order terms in the free energy because they will only result in some quantitative changes [8]. As Landau and Ginzburg have argued, near the continuous transition point Eq. (14) can be re-expressed with coupled fields, leading to the free energy density

$$f = f_0 + \frac{1}{2} [(\nabla \phi)^2 + r \phi^2] + u \phi^4 + v \sum_{i=1}^2 (\phi_i)^4, \quad (15)$$

where  $\phi^2 = \sum_{i=1}^2 (\phi_i)^2$  and  $(\nabla \phi)^2 = \sum_{i=1}^2 (\nabla \phi_i)^2$ , representing the kinetic term. Because of  $\mathcal{F} = -k_B T \log \mathcal{Z}$ , where

$$\mathcal{Z} = \int \mathcal{D}\vec{\phi} e^{-\beta \mathcal{H}[\vec{\phi}]}, \quad (16)$$

is the partition function, we can see that Eq. (15) turns out corresponding to the integrand in Eq. (13) with only two components instead of three. A recent work by Venus utilizing RG upon 2D XY model with fourfold anisotropy reveals that the finite-size Kosterlitz-Thouless (KT) transition takes place with weak anisotropy, while a crossover to the Ising criticality happens as the strength of anisotropy increases [34]. The existence of KT transition also implies that there is a quasi-ordered phase between the high-temperature paramagnetic phase and the low-temperature ferromagnetic phase [35]. As a result, starting from the  $C$  phase near the phase boundary in zero temperature (recall that the anisotropy needs to be weak), our 2D lattice model can feasibly host two KT transitions in finite temperature. We will leave the further investigation for future studies.

### 2. Quantum phase transition

In zero temperature our MFA and iPEPS calculations reveal two phase boundaries of quantum phase transition (QPT). In the general form of quantum field theory (QFT), we write down the corresponding Lagrangian density

$$\begin{aligned} \mathcal{Z} &= \int \mathcal{D}\Psi \mathcal{D}\Psi^* \exp \left( - \int d\tau d^d x \mathcal{L} \right), \\ \mathcal{L} &= K_1 \Psi^* \frac{\partial \Psi}{\partial \tau} + K_2 \left| \frac{\partial \Psi}{\partial \tau} \right|^2 - \frac{1}{2} [|\nabla \Psi|^2 + r |\Psi|^2] \\ &\quad - u |\Psi|^4 - v \sum_{i=1}^2 |\Psi_i|^4, \end{aligned} \quad (17)$$

where  $\Psi = \Phi_1 + i\Phi_2$  stands for the order parameter and  $\tau$  is the imaginary time. Since Eq. (17) must be unchanged under the transformation of  $(\Phi_1, \Phi_2) \rightarrow (\Phi_2, \Phi_1)$  (the symmetry in Eq. (1)), its Lagrangian density finally becomes

$$\begin{aligned} \mathcal{L} &= K_1 \sum_{i=1}^2 \Phi_i \frac{\partial \Phi_i}{\partial \tau} + K_2 \left| \frac{\partial \Psi}{\partial \tau} \right|^2 - \frac{1}{2} [|\nabla \Psi|^2 + r |\Psi|^2] \\ &\quad - u |\Psi|^4 - v \sum_{i=1}^2 |\Psi_i|^4. \end{aligned} \quad (18)$$

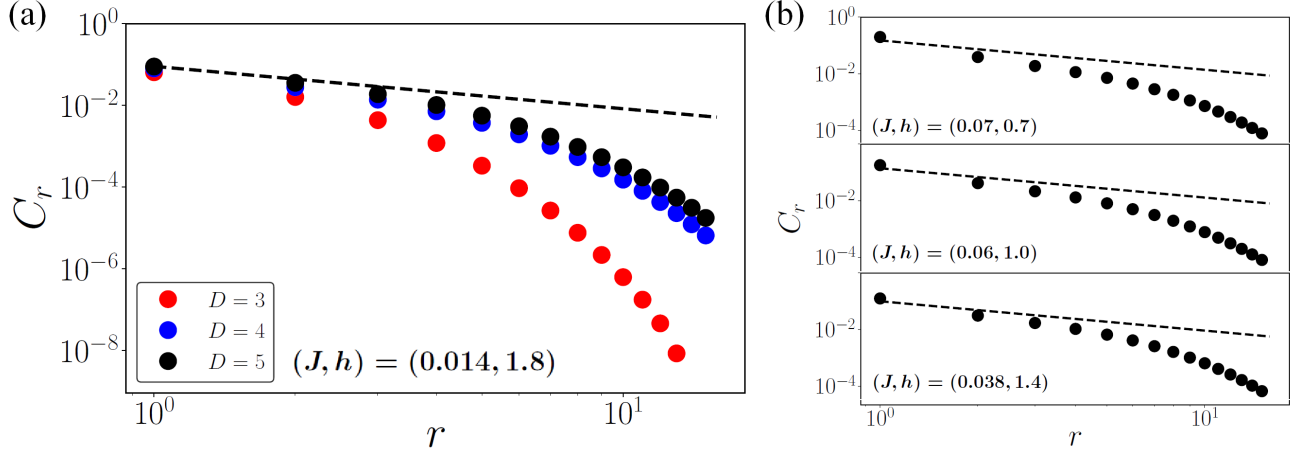


FIG. 6. Correlation functions in log-log scale at different points on the estimated phase boundary. Results of  $(D, \chi) = (5, 50)$ ,  $(4, 70)$ , and  $(3, 100)$  are provided for  $(J, h) = (0.014, 1.8)$  in (a), while the samplings for other points with  $(D, \chi) = (5, 50)$  are also shown in (b). Dashed lines represent the power-law decay of correlation function in 3D XY criticality with  $\eta = 0.038$ .

Neglecting the anisotropy term ( $v = 0$ ), Eq. (18) represents the standard model for the dilute Bose gas [36]. It is well-known that as long as  $K_1 \neq 0$ ,  $K_2$  becomes irrelevant after rescaling; therefore we end up with a dynamical critical exponent  $z = 2$ . With  $d = 2$ , the QFT lies right on the upper critical dimension for the quartic field term. Moreover, at the multicritical point where the particle-hole symmetry is present,  $K_1 = 0$  and thus  $z = 1$  [37]. Notably, as  $z = 1$  the QFT becomes Lorentz-invariant, meaning that the imaginary time can be treated as an independent extra dimension.

Although it is not straightforward to deduce whether  $z = 1$  or 2 when the anisotropy is present, the nature of our phase transition provides us further clue. As we have argued, the effect of anisotropy is manifest away from the phase boundary in the  $C$  phase, leading to an ordered state breaking a discrete symmetry group; therefore it is a gapped phase. Since the  $P$  phase is also gapped, crossing the phase boundary the gap closes and re-opens again, whose energy dispersion is the most likely linear around the  $\Gamma$  point under the gap closure. Here we emphasize that it does not contradict with the  $U(1)$ -symmetry emergence because unless we sit on the critical point where the anisotropy can become truly irrelevant, its effect cannot be strictly ignored elsewhere, leading to a non-zero gap everywhere in the symmetry-breaking  $C$  phase. Since the linear dispersion implies the Lorentz-invariance, because the space (reciprocal to the momentum) and time (reciprocal to the energy) dimensions play the same role, we deduce that the first term of Eq. (18) would disappear. As a result, Eq. (18) corresponds to Eq. (13) with two components in three dimensions, suggesting that the  $U(1)$  symmetry emerges at the transition points and the criticality is governed by the 3D XY universality class.

Here we provide a numerical evidence in supporting our deduction. In studying the quantum criticality, some important information can be extracted from the connected correlation

function

$$C_r = \sum_{\alpha} \langle S_0^{\alpha} S_{r\hat{x}}^{\alpha} \rangle - M_{\alpha}^2, \quad (19)$$

where  $\alpha = x, y$ . Right on the critical point the correlation length ( $\xi$ ) diverges and  $C_r$  scales as

$$C_r \sim r^{-d+2-\eta}, \quad (20)$$

where  $\eta$  is the critical exponent of correlation function. Despite the fact that the finite- $D$  iPEPS is never able to capture the divergence of  $\xi$ , within the short range we can still approximate  $\eta$  [38, 39].

In Fig. 6(a) we provide the log-log plots of  $C_r$  for  $(J, h) = (0.014, 1.8)$  with three different  $D$ . Note that  $(D, \chi) = (5, 50)$  already reaches the maximal set-up within our machine's capacity. Dashed lines represent the function of Eq. (20) with  $\eta = 0.038$ , which is the critical exponent for the 3D XY universality class. We can see that as  $D$  increases the simulated curve of  $C_r$  moves toward the dashed line and for  $D = 5$ , a nice fitting along that line for small  $r$  is captured. We have also sampled some other points in Fig. 6(b) and all of the results seem to indicate the liability that they belong to the same universality class. As a consequence, our numerical results also root for the picture of an emergent  $U(1)$  symmetry and a Lorentz-invariant criticality. In sum, from both the theoretical analysis and numerical data, we have proper reasons to be convinced that our phase boundary is governed by the 3D XY universality class.

### C. Application

Our results and analysis so far indicate that near the phase boundary  $U(1)$  symmetry gradually emerges, resulting in the phenomenon of easy-axis softening. This discovery provides a new possibility in manipulating the magnetism of diluted

magnetic semiconductor (DMS) [5], where such manipulation plays an important role in designing new devices for future spintronics [40]. In the earlier studies, through applying an external electric field the magnetic easy axis can be shifted due to the altering of carrier concentration led by the field [41–44]. For the spin model that we study here, the Mn-doped gallium phosphide ceramic,  $\text{Ga}_{1-x}\text{Mn}_x\text{P}$ , provides a good platform in its realization. GaP has the neutral Mn acceptor ( $\text{Mn}^{3+}$ ) with spin  $S = 2$  [45] as well as the ferromagnetic exchange [46], whose Curie temperature (and thus the strength of superexchange coupling) can be adjusted by the Mn concentration [47]. Under a low temperature, moreover, it has a  $\langle 011 \rangle$  cubic anisotropy along with a negligible in-plane uniaxial anisotropy, leading to an easy axis close to  $[01\bar{1}]$  [48, 49]. We believe that our proposal here can be used to describe the physical scenario of a well-doped  $\text{Ga}_{1-x}\text{Mn}_x\text{P}_{1-y}\text{N}_y$  with a  $\theta = \pi/4$  easy axis. By casting a controlled external magnetic field  $\mathbf{h}||[100]$ , we first pin down a strength which does not fully polarize the magnetization, yet the easy-axis softening is manifest. After that, we can manipulate the magnetism by applying a small in-plane field, without the need to change the intrinsic properties of the materials.

From Ref. [48] we notice that the contribution of cubic anisotropy decreases rapidly after 5 Kelvin, suggesting that this easy-axis softening might be observed in a very low temperature. An easy way to investigate this phenomenon is to detect the angular dependence of ferromagnetic resonance field under a perpendicular external magnetic field [48], which has, to the best of our knowledge, not been done by any group yet. In sum, the easy-axis softening introduced here unveils a new possibility in manipulating the magnetism for spinful semiconductors, leading to a potential usage for future semiconductor devices.

#### IV. CONCLUSION

In this work we study a lattice spin model composed of the ferromagnetic Heisenberg term and a cubic anisotropy under a nonzero magnetic field. Utilizing the 2D iPEPS tensor network ansatz, we obtain a more accurate phase diagram than the one by MFA in the quantum regime. Despite a four-fold degeneracy of magnetization in the canted phase resulting from the anisotropy, our discovery indicates an easy-axis softening near the critical phase boundary, signifying an emergent  $U(1)$  symmetry. Combining the perspective of field theory and iPEPS results, the  $U(1)$  symmetry feasibly becomes exact right on the phase boundary and the criticality belongs to the 3D XY universality class. Besides the theoretical interest, such an effect also underlines some crucial practical applications upon 2D magnetic thin films in low temperature and we look forward to experimental studies for further confirmation.

At last, we point out two promising directions for future works. First, a further confirmation of the critical nature is appreciable. While the QMC calculation is hindered for this lattice model, a direct derivation of its QFT from the path integral representation or adopting the conformal field theory could be the liable candidate in validating our current scope.

Second, informed by the recent work [34] that a 2D XY model with anisotropy can host a finite-temperature KT transition, to study the finite-temperature behavior of our model is also favorable. Since we have a lattice spin model, it is more suitable in describing the micro-mechanism of a 2D ferromagnetic thin film. By adopting the thermal state purification through iPEPS and infinite projected entangled-pair operator (iPEPO), its behavior in finite temperature can be probed [50, 51], providing us with further information.

In sum, although Eq. (1) is just the simplest spin model of Heisenberg ferromagnet with cubic anisotropy, it already contains a huge potential which has not been fully exploited and thus merits future studies. We hope that our discoveries here can push further people’s understanding upon the magnetic anisotropy which is quite ubiquitous but yet mysterious.

#### V. ACKNOWLEDGEMENT

Authors appreciate decent comments and discussion from Eun-Gook Moon, Jun Takahashi, and Tsuyoshi Okubo. Part of the calculation was conducted in the Supercomputer Center of ISSP, the University of Tokyo. W.-L.T. and H.-Y.L. are supported by National Research Foundation of Korea under the grant numbers NRF-2020R111A3074769. H.-Y.L. was supported by Basic Science Research Program through the National Research Foundation of Korea (NRF) funded by the Ministry of Education (2014R1A6A1030732). X.L. is grateful to the support of the Global Science Graduate Course (GSGC) program of the University of Tokyo. S.R.G. and N.K. are supported by JSPS KAKENHI Grant No. JP19H01809. H.-K.W. is supported by JQI-NSF-PFC (NSF Grant No. PHY-1607611).

#### VI. AUTHOR CONTRIBUTION

N.K. conceived the topic in the first place. W.-L.T., X.L., and S.R.G. collaborated in providing numerical results, and the latter two co-authors share the same amount of work. W.-L.T., H.-Y.L., and N.K. worked on its theoretical insight. H.-K.W. provided some assistance for the numerical calculation.

#### Appendix A: The difficulty in applying QMC

As many of the physicists would have agreed, when handed with a many-body model on the lattice, QMC is one of the most reliable numerical tools that we can think of [52, 53]. It has demonstrated its strength in many aspects [54], such as probing the various deconfined quantum criticality which is still an active research field [55–59]. However, due to the vicious sign problem [60] it hinders the utility of QMC upon many correlated systems of more interest. The origin of sign problem comes from the negative weight of a configuration which could happen in a system with frustration or a fermionic system. In general, if the negative sign of our Hamiltonian,

$-H$ , has negative off-diagonal elements, it is likely to cause the sign problem.

For our lattice model (Eq. (1)), we have known that the Heisenberg term causes no sign problem in the square lattice, nor the Zeeman term. For the  $K$  term, it can be expanded by the  $S = 2$  operators and the result is

$$-\sum_{\alpha}(S^{\alpha})^4 = \begin{bmatrix} -21 & & & -3 \\ & -18 & & \\ & & -24 & \\ -3 & & & -18 \\ & & & & -21 \end{bmatrix}. \quad (\text{A1})$$

One can see that we have negative off-diagonal terms and thus negative weights of some configuration might appear. However, in the conventional world-line QMC, summing up all possible world-line configurations for the partition function, the periodic boundary condition along the direction of imaginary time force the action of  $K$  term being an even number. As a result, we can dodge the bullet of sign problem.

Nevertheless, an obscure difficulty will happen for our model. As mentioned above, in QMC one needs to determine the weight for each world-line configuration in order to construct the partition function, and the standard way is by putting the configuration through a Markov process, where the configuration goes through a series of local flips [61]. Shown in Eq. (A1), on the other hand, the  $K$  term could flip the  $|2\rangle$  state into  $|-2\rangle$  at each site, while it demands at least four times of acting  $J$  term in order to connect these two states. This will make some processes, such as creating  $|2\rangle$  at one site while annihilating it at another site, very complicated and result in a world-line configuration that is hard to equilibrate, while such processes are doomed to happen in the  $C$  phase. Even taking into account the more efficient loop update or worm algorithm, this obstacle still remains. So far we are not aware of any QMC algorithm that could resolve this issue.

## Appendix B: infinite projected entangled pair states

### 1. iPEPS basics

Due to the difficulty in applying QMC, in this work we make use of the infinite projected entangled pair states (iPEPS), which is a variational tensor network ansatz for approximating the ground state of a two dimensional quantum systems in the thermodynamic limit [15–17], in order to study our system beyond MFA. Obeying the area law, absence of sign problem and lattice size augmentation put iPEPS among one of the most desirable computational methods in many-body physics especially for strongly correlated systems. The basic idea in iPEPS consists of considering a repeating unit cell of interconnected tensors, so called the bulk tensors, and simulating an effective environment by constructing a series of border tensors. Each bulk tensor encodes the entanglement with its neighboring sites by having four virtual bonds with bond dimension equal to  $D$ , along with one physical index which reflects the local Hilbert space dimension ( $d = 5$  in this work). Since we consider a ferromagnetic system in a

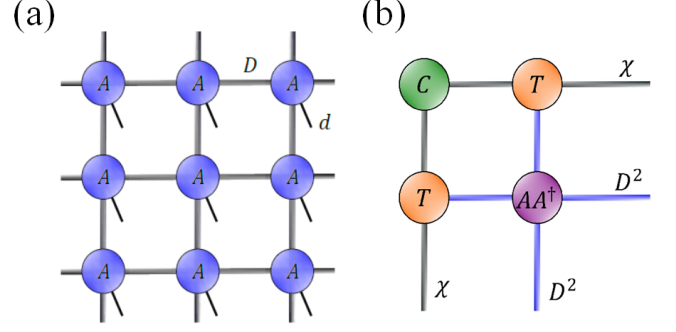


FIG. 7. (a) iPEPS scheme with rank-5 tensors on each lattice site where thick and thin solid lines represent virtual ( $D$ ) and physical ( $d$ ) bonds respectively. (b) Corner ( $C$ ), edge ( $T$ ) and double layer ( $AA^\dagger$ ) tensors in the upper-left corner. Grey bonds possess dimension equal to  $\chi$  which in general should be no smaller than  $D^2$ , and the dimension for blue bonds is  $D^2$ .

square lattice, it then has a  $1 \times 1$  repeating unit cell as shown in Fig. 7(a).

In order to compute the norm and the observables we then contract the tensor ( $A$ ) to its complex conjugate ( $A^\dagger$ ) and trace out the physical bond so that it results in a double-layer tensor ( $AA^\dagger$ ). This tensor object becomes the basic block while we approximate the environment tensors through the corner transfer matrix renormalization group (CTMRG) procedure [62–64]. Since the computational cost for the exact contraction of a 2D network exponentially grows along with the size, we construct the projector tensors through truncation after singular-value decomposing a tensor bond [64]. Once the CTMRG converges, we obtain the corner  $C$  and edge  $T$  tensors as depicted in Fig. 7(b). By constructing the environment tensors around the bulk tensor we can extrapolate the system size to the thermodynamic limit and calculate the energy or desired physical observables.

As a variational ansatz, various optimization methods based on the imaginary time evolution (ITE) such as simple [15], full [65] and fast-full updates [66] have already been proposed and implemented for oftentimes. On the other hand, although it is not an easy task to evaluate the energy gradient of each variational parameter [67, 68], a breakthrough in optimizing iPEPS emerged by adopting the idea of automatic differentiation (AD) [69], which has been employed for optimizing problems with a large number of parameters and already proved its efficiency in many neural network studies. An advanced optimization scheme combining both ITE and AD has also been proposed recently [70].

In this work, we adopt the variational optimization using AD for our ansatz. The objective in AD optimization is to record down the computation graph from initial bulk tensors to the final energy estimation (see the Method Section in Ref. [71]). After completing one computation flow (one epoch), the energy gradients are evaluated through the backward propagation; hence we can make use of these gradients to update the tensor elements (variational parameters) with a desired degree (learning rate), until a desirable convergence is achieved. We can then utilize the converged ansatz for further

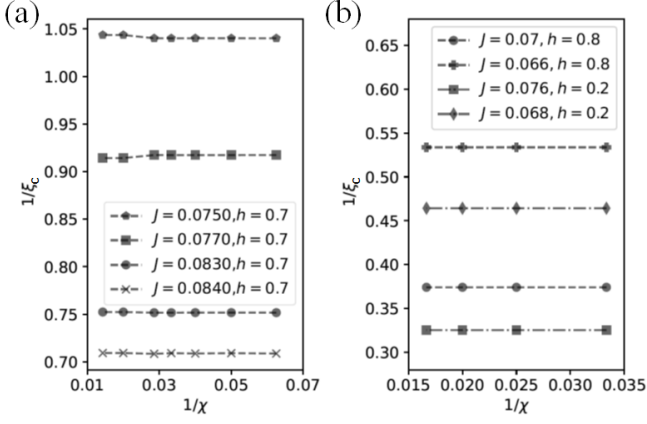


FIG. 8. We plot the characteristic  $\xi$  obtained by Eq. (B1) for different  $\chi$  in (a)  $D = 3$  and (b)  $D = 4$ . From the data we can see that the variance of value in  $\xi$  along  $\chi$  is negligible.

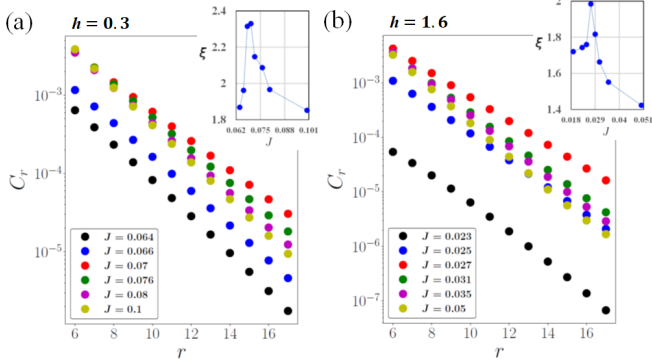


FIG. 9. The  $\log$ - $r$  plots for  $C_r$  ( $D = 4$ ,  $\chi = 70$ ) along the vertical cuts at (a)  $h = 0.3$  ( $J_c \sim 0.07$ ) and (b)  $h = 1.6$  ( $J_c \sim 0.027$ ). Inset in each plot shows the estimated  $\xi$  which is equal to the inverse minus slope of  $\log(C_r)$  in the long range for different  $J$ .

calculation of physical observables. In this work, we adopt a practical package, `peps-torch` [72], for our calculation. Previously, this package has demonstrated a very good capability for various spin systems such as frustrated Heisenberg antiferromagnet [39, 73], chiral spin liquid [74], and novel quantum magnetism [71], as well as the bosonic system [75].

## 2. Transition points by iPEPS

While iPEPS is an effective tensor network ansatz in two dimensions, its limitation lies on the available size of bond dimension. Despite the fact that by utilizing the global symmetries of tensor network ansatz we are able to enlarge the bond dimension [38, 39, 76–78], because of the lacking of desirable symmetry in our model it does not seem to be feasible and thus our calculation is constrained to smaller bond dimensions. For our study using full tensors, the maximum setup which is affordable for our machine is  $(D, \chi) \approx (5, 50)$ .

Because of the limitation, in this work we only provide the

phase boundary estimated by finite  $D$  without extrapolation to  $D \rightarrow \infty$ . However, from Fig. 2 we also see that the estimated transition points barely change after  $D = 4$ , fortifying the reliability of our phase diagram. On the other hand, it is well-known that finite- $D$  iPEPS tends to over-emphasize the values of order parameter. Without extrapolation a discontinuous behavior is likely captured by iPEPS calculation, blurring the accurate transition points. As a consequence, in this work we adopt the correlation length,  $\xi$ , as the indicator of continuous phase transition.

Since the finite- $D$  iPEPS can only capture the gapped phase, the estimated  $\xi$  can never diverge even on the critical point. However, near the continuous phase boundary we can still witness the “rising up” feature of  $\xi$ , despite the fact that it never goes to the infinity [79]. To estimate  $\xi$ , one way we can follow is to construct the transfer matrix after the ansatz has converged and the ratio of its two leading eigenvalues represents the information of characteristic correlation length  $\xi_c$  [38, 39]

$$\xi_c = -\frac{1}{\log|\lambda_1/\lambda_0|}, \quad (\text{B1})$$

where the eigenvalues follow the descending order  $|\lambda_0| > |\lambda_1| > |\lambda_2| \dots$ . However, for the finite- $D$  iPEPS we cannot ignore the effect from the third (or even higher order) leading eigenvalue, and thus an effective extrapolation formula has been proposed [80]. Unfortunately, as shown in Fig. 8 without adopting a very large  $\chi$ , the estimated  $\xi_c$  barely changes and thus we are not able to apply the extrapolation formula. Fig. 8 also conveys the message that within the available values of  $\chi$ , the results of simulation are scarcely altered.

Instead of probing  $\xi_c$  from the transfer matrix, in this article we estimate the values of correlation length from the correlation function,  $C_r$ , because the observables already converge well with smaller  $\chi$  [78, 79]. In the longer range where exponentially decay of  $C_r$  takes place, it scales as

$$C_r \sim e^{-r/\xi}, \quad (\text{B2})$$

and thus the inverse minus slope of  $\log(C_r)$ - $r$  plot for  $r \gg 1$  provides us with the estimated value of  $\xi$ . According to the previous studies  $\xi$  and  $\xi_c$  should share similar values after a well estimation [38].

In Fig. 9 we demonstrate the  $\log(C_r)$ - $r$  plots for the correlation function at different points along the vertical cut at  $h = 0.3$  (1.6). We can see that the red dots decrease the slowest and it represents  $J = 0.07$  ( $J = 0.027$ ). In the insets we show the estimated  $\xi$  and indeed there is a summit around the two points; as a consequence the critical points can be approximated. By repeating the same procedure for different vertical cuts we end up producing the phase diagram in Fig. 2.

## Appendix C: Effective hard-core bosonic model

In Section III A we present an effective Hamiltonian of HCB from the low-energy  $H_f^{\text{eff}}$  and we will show the deriva-

tion here. First, re-write Eq. (10) into

$$H_J^{\text{eff}} = -2JN^2 \sum_{\langle i,j \rangle} \sigma_i^+ \sigma_j^- + \sigma_j^+ \sigma_i^- - J \sum_{\langle i,j \rangle} (\gamma_1 \sigma_i^z + \gamma_2 \mathbb{1}_i)(\gamma_1 \sigma_j^z + \gamma_2 \mathbb{1}_j), \quad (\text{C1})$$

with  $\gamma_1 = N^2(1 - \alpha^2) - \frac{1}{2}$ ,  $\gamma_2 = N^2(1 - \alpha^2) + \frac{1}{2}$ , and  $\mathbb{1}$  stands for the identity matrix. After expanding Eq. (C1), we obtain

$$H_J^{\text{eff}} = -2JN^2 \sum_{\langle i,j \rangle} \sigma_i^+ \sigma_j^- + \sigma_j^+ \sigma_i^- - J\gamma_1^2 \sum_{\langle i,j \rangle} \sigma_i^z \sigma_j^z - 4J\gamma_1\gamma_2 \sum_i \sigma_i^z, \quad (\text{C2})$$

where the  $\mathbb{1}_i \mathbb{1}_j$  term has been ignored since it only contribute a constant energy. By assigning  $t_J = 2JN^2$ ,  $V_J = -J\gamma_1^2$ , and  $B_J = 4J\gamma_1\gamma_2$ , we obtain the Hamiltonian in Eq. (12).

#### Appendix D: RG flow in the leading order

In this Appendix we will demonstrate the perturbative RG flow of Eq. (13). After performing the  $\epsilon$ -expansion to the leading order, we obtain the following flow equations

$$\begin{aligned} \frac{dr}{dl} &= 2r + 4[(n+2)u + 3v] \frac{K_d \Gamma^d}{\Gamma^2 + r}, \\ \frac{du}{dl} &= \epsilon u - 4[(n+8)u^2 + 6uv] \frac{K_d \Gamma^d}{(\Gamma^2 + r)^2}, \\ \frac{dv}{dl} &= \epsilon v - 4(9v^2 + 12uv) \frac{K_d \Gamma^d}{(\Gamma^2 + r)^2}, \end{aligned} \quad (\text{D1})$$

where  $\Gamma$  stands for the highest frequency in the  $d$ -dimensional momentum space and  $K_d$  is the solid angle of the  $d$ -dimensional sphere divided by  $(2\pi)^d$ .  $\delta l$  is the re-scaling of  $\Gamma \rightarrow \Gamma/b$  with  $b = 1 + \delta l$ . Since the flow of  $r$  represents the high- and low-temperature fixed points, we only need to consider the flows of  $u$  and  $v$  when searching for different fixed points, and they exist as  $du/dl = dv/dl = 0$  (setting  $r = 0$ )

$$\begin{aligned} \{\epsilon - 4[(n+8)u^* + 6v^*]K_d\Gamma^{d-4}\}u^* &= 0, \\ \{\epsilon - 4(9v^* + 12u^*)K_d\Gamma^{d-4}\}v^* &= 0. \end{aligned} \quad (\text{D2})$$

From now on we will set  $\kappa = K_d\Gamma^{d-4}$ . As a result, we have four fixed points

$$\begin{aligned} \text{Gaussian} : u_G^* &= v_G^* = 0, \\ O(n) : u_O^* &= \frac{\epsilon}{4\kappa(n+8)} \quad \text{and} \quad v_O^* = 0, \\ \text{Ising} : u_I^* &= 0 \quad \text{and} \quad v_I^* = \frac{\epsilon}{36\kappa}, \\ \text{cubic} : u_C^* &= \frac{\epsilon}{12\kappa n} \quad \text{and} \quad v_C^* = \frac{\epsilon(n-4)}{36\kappa n}. \end{aligned} \quad (\text{D3})$$

Besides the trivial Gaussian fixed point, other three fixed points all possess an “eigendirection” along which the flow goes toward themselves.  $O(n)$  fixed point takes place at  $v = 0$  where Eq. (13) resumes to be the  $n$ -vector model enjoying the  $O(n)$  symmetry. On the other hand, as  $u = 0$  a fixed point corresponding to  $n$  copies of decoupled Ising models is located at  $v_I^*$ , and is therefore called the Ising fixed point. The only fixed point that demands non-zero values for both  $u$  and  $v$  is the cubic fixed point that we wish to have and the next step is to examine their stability. Notice that when  $n = 4$  the  $O(n)$  and cubic fixed points become the same. Around the vicinity of each fixed point, their stability can be verified by solving the following eigen-problem

$$\begin{aligned} \frac{d}{dl} \begin{bmatrix} \delta u \\ \delta v \end{bmatrix} &= \mathbf{M} \begin{bmatrix} \delta u \\ \delta v \end{bmatrix}, \\ \mathbf{M} &= \begin{bmatrix} \epsilon - 8\kappa[(n+8)u^* + 3v^*] & -24\kappa u^* \\ -48\kappa v^* & \epsilon - 24\kappa[2u^* + 3v^*] \end{bmatrix}. \end{aligned} \quad (\text{D4})$$

Near each fixed points, Eq. (D4) provides two eigenvalues which we can make use of to construct the RG flow:

$$\begin{aligned} \text{Gaussian} : \lambda_G^1 &= \lambda_G^2 = \epsilon, \\ O(n) : \lambda_O^1 &= -\epsilon \quad \text{and} \quad \lambda_O^2 = \frac{n-4}{n+8}\epsilon, \\ \text{Ising} : \lambda_I^1 &= \frac{1}{3}\epsilon \quad \text{and} \quad \lambda_I^2 = -\epsilon, \\ \text{cubic} : \lambda_C^1 &= -\epsilon \quad \text{and} \quad \lambda_C^2 = \frac{4-n}{3n}\epsilon. \end{aligned} \quad (\text{D5})$$

The full flow diagram has been plotted in many previous works [27, 28, 81, 82] and textbooks [83–86]. An important feature of the flow diagram is that there is a critical value for its component above or below which the stable fixed point would change. Indeed, from Eq. (D5) we can clearly see that when  $n < 4$  the  $O(n)$  fixed point is always stable while it is the case for the cubic fixed point as  $n > 4$ . Thus, we have a critical value of component ( $n_c$ ), which determines the stable fixed point and is equal to 4 in the leading-order expansion.

[1] J. H. van Vleck, On the Anisotropy of Cubic Ferromagnetic Crystals, *Phys. Rev.* **52**, 1178 (1937).

[2] B. D. Cullity and C. D. Graham, *Introduction to Magnetic Materials, Second Edition* (Wiley, 2008).

[3] K. F. Mak, J. Shan, and D. C. Ralph, Probing and controlling magnetic states in 2D layered magnetic materials, *Nat. Rev. Phys.* **1**, 646 (2019).

[4] T. Dietl, A ten-year perspective on dilute magnetic semiconductors and oxides, *Nat. Mater.* **9**, 965 (2010).

- [5] T. Dietl and H. Ohno, Dilute ferromagnetic semiconductors: Physics and spintronic structures, *Rev. Mod. Phys.* **86**, 187 (2014).
- [6] S. K. Sinha, G. H. Lander, S. M. Shapiro, and O. Vogt, Neutron scattering investigation of the phase transitions in uranium arsenide, *Phys. Rev. B* **23**, 4556 (1981).
- [7] J. Sznajd, Tricritical points in ferromagnets with cubic single-ion anisotropy, *J. Magn. Magn. Mater.* **42**, 269 (1984).
- [8] Z. Domański and J. Sznajd, Phase Diagrams of Ferromagnets with Cubic Single-Ion Anisotropy, *Phys. Status Solidi B* **129**, 135 (1985).
- [9] A. I. Mitsek, K. Y. Guslienko, and S. V. Pavlovskii, Electron structure and phase diagrams of low-temperature rare-earth magnets, *Phys. Status Solidi B* **135**, 173 (1986).
- [10] Z. Domański and J. Sznajd, Field-induced phase transitions in ferromagnets with cubic single-ion anisotropy, *Journal of Magnetism and Magnetic Materials* **71**, 306 (1988).
- [11] J. Sznajd and M. Dudziński, Nature of a phase transition and low-temperature phase in cubic ferromagnets, *Phys. Rev. B* **59**, 4176 (1999).
- [12] M. Dudziński and J. Sznajd, Quadrupolar order in the Heisenberg ferromagnet with the single-ion cubic anisotropy, *Eur. Phys. J. B* **5**, 745 (1998).
- [13] M. Dudziński, G. Fáth, and J. Sznajd, Magnetic and quadrupolar order in a one-dimensional ferromagnet with cubic crystal-field anisotropy, *Phys. Rev. B* **59**, 13764 (1999).
- [14] M. Dudziński, J. Sznajd, and J. Zittartz, Quadrupolar order in the  $S = 2$  Heisenberg ferromagnet with the single-ion cubic anisotropy, *Eur. Phys. J. B* **17**, 575 (2000).
- [15] J. Jordan, R. Orús, G. Vidal, F. Verstraete, and J. I. Cirac, Classical Simulation of Infinite-Size Quantum Lattice Systems in Two Spatial Dimensions, *Phys. Rev. Lett.* **101**, 250602 (2008).
- [16] R. Orús, Tensor networks for complex quantum systems, *Nat. Rev. Phys.* **1**, 538 (2019).
- [17] J. I. Cirac, D. Pérez-García, N. Schuch, and F. Verstraete, Matrix product states and projected entangled pair states: Concepts, symmetries, theorems, *Rev. Mod. Phys.* **93**, 045003 (2021).
- [18] J. V. José, L. P. Kadanoff, S. Kirkpatrick, and D. R. Nelson, Renormalization, vortices, and symmetry-breaking perturbations in the two-dimensional planar model, *Phys. Rev. B* **16**, 1217 (1977).
- [19] D. Blankschtein, M. Ma, A. N. Berker, G. S. Grest, and C. M. Soukoulis, Orderings of a stacked frustrated triangular system in three dimensions, *Phys. Rev. B* **29**, 5250 (1984).
- [20] M. Oshikawa, Ordered phase and scaling in  $Z_n$  models and the three-state antiferromagnetic Potts model in three dimensions, *Phys. Rev. B* **61**, 3430 (2000).
- [21] M. E. Fisher, The renormalization group in the theory of critical behavior, *Rev. Mod. Phys.* **46**, 597 (1974).
- [22] K. G. Wilson, The renormalization group and critical phenomena, *Rev. Mod. Phys.* **55**, 583 (1983).
- [23] M. E. Fisher, Renormalization group theory: Its basis and formulation in statistical physics, *Rev. Mod. Phys.* **70**, 653 (1998).
- [24] J. C. Slonczewski and H. Thomas, Interaction of Elastic Strain with the Structural Transition of Strontium Titanate, *Phys. Rev. B* **1**, 3599 (1970).
- [25] A. Aharony, Critical Behavior of Anisotropic Cubic Systems, *Phys. Rev. B* **8**, 4270 (1973).
- [26] K. G. Wilson and J. Kogut, The renormalization group and the  $\epsilon$  expansion, *Physics Reports* **12**, 75 (1974).
- [27] J. Manuel Carmona, A. Pelissetto, and E. Vicari,  $n$ -component Ginzburg-Landau Hamiltonian with cubic anisotropy: A six-loop study, *Phys. Rev. B* **61**, 15136 (2000).
- [28] L. T. Adzhemyan, E. V. Ivanova, M. V. Kompaniets, A. Kudlis, and A. I. Sokolov, Six-loop  $\epsilon$  expansion study of three-dimensional  $n$ -vector model with cubic anisotropy, *Nuclear Physics B* **940**, 332 (2019).
- [29] M. Hasenbusch and E. Vicari, Anisotropic perturbations in three-dimensional  $O(N)$ -symmetric vector models, *Phys. Rev. B* **84**, 125136 (2011).
- [30] S. M. Chester, W. Landry, J. Liu, D. Poland, D. Simmons-Duffin, N. Su, and A. Vichi, Bootstrapping Heisenberg magnets and their cubic instability, *Phys. Rev. D* **104**, 105013 (2021).
- [31] R. Moessner and S. L. Sondhi, Ising models of quantum frustration, *Phys. Rev. B* **63**, 224401 (2001).
- [32] S. V. Isakov and R. Moessner, Interplay of quantum and thermal fluctuations in a frustrated magnet, *Phys. Rev. B* **68**, 104409 (2003).
- [33] Y.-C. Wang, Y. Qi, S. Chen, and Z. Y. Meng, Caution on emergent continuous symmetry: A monte carlo investigation of the transverse-field frustrated ising model on the triangular and honeycomb lattices, *Phys. Rev. B* **96**, 115160 (2017).
- [34] D. Venus, Renormalization group analysis of the finite two-dimensional XY model with fourfold anisotropy: Application to the magnetic susceptibility of a ferromagnetic ultrathin film, *Phys. Rev. B* **105**, 235440 (2022).
- [35] Z.-Q. Li, L.-P. Yang, Z. Y. Xie, H.-H. Tu, H.-J. Liao, and T. Xiang, Critical properties of the two-dimensional  $q$ -state clock model, *Phys. Rev. E* **101**, 060105 (2020).
- [36] S. Sachdev, *Quantum Phase Transitions* (Cambridge University Press, 2016) p. 293–331.
- [37] M. P. A. Fisher, P. B. Weichman, G. Grinstein, and D. S. Fisher, Boson localization and the superfluid-insulator transition, *Phys. Rev. B* **40**, 546 (1989).
- [38] R. Haghshenas and D. N. Sheng,  $U(1)$ -symmetric infinite projected entangled-pair states study of the spin-1/2 square  $J_1 - J_2$  heisenberg model, *Phys. Rev. B* **97**, 174408 (2018).
- [39] J. Hasik, D. Poilblanc, and F. Becca, Investigation of the Néel phase of the frustrated Heisenberg antiferromagnet by differentiable symmetric tensor networks, *SciPost Phys.* **10**, 12 (2021).
- [40] H. Ohno, A window on the future of spintronics, *Nat. Mater.* **9**, 952 (2010).
- [41] H. Ohno, D. Chiba, F. Matsukura, T. Omiya, E. Abe, E. Dietl, Y. Ohno, and K. Ohtani, Electric-field control of ferromagnetism, *Nature (London)* **408**, 944 (2000).
- [42] D. Chiba, M. Yamanouchi, F. Matsukura, and H. Ohno, Electrical Manipulation of Magnetization Reversal in a Ferromagnetic Semiconductor, *Science* **301**, 943 (2003).
- [43] D. Chiba, M. Sawicki, Y. Nishitani, Y. Nakatani, F. Matsukura, and H. Ohno, Magnetization vector manipulation by electric fields, *Nature (London)* **455**, 515 (2008).
- [44] F. Matsukura, Y. Tokura, and H. Ohno, Control of magnetism by electric fields, *Nat. Nano* **10**, 209 (2015).
- [45] J. Kreissl, W. Ulrici, M. El-Metoui, A.-M. Vasson, A. Vasson, and A. Gavaix, Neutral manganese acceptor in GaP: An electron-paramagnetic-resonance study, *Phys. Rev. B* **54**, 10508 (1996).
- [46] M. A. Scarpulla, B. L. Cardozo, R. Farshchi, W. M. H. Oo, M. D. McCluskey, K. M. Yu, and O. D. Dubon, Ferromagnetism in  $\text{Ga}_{1-x}\text{Mn}_x\text{P}$ : Evidence for Inter-Mn Exchange Mediated by Localized Holes within a Detached Impurity Band, *Phys. Rev. Lett.* **95**, 207204 (2005).
- [47] Y. Yuan, Y. Wang, M. Khalid, K. Gao, S. Prucnal, O. D. Gordan, G. Salvan, D. R. T. Zahn, W. Skorupa, M. Helm, and S. Zhou, Ferromagnetic GaMnP Prepared by Ion Implantation and Pulsed Laser Annealing, *IEEE Transactions on Magnetics* **50**, 1 (2014).

- [48] C. Bihler, M. Kraus, H. Huebl, M. S. Brandt, S. T. B. Goennenwein, M. Opel, M. A. Scarpulla, P. R. Stone, R. Farshchi, and O. D. Dubon, Magnetocrystalline anisotropy and magnetization reversal in  $\text{Ga}_{1-x}\text{Mn}_x\text{P}$  synthesized by ion implantation and pulsed-laser melting, *Phys. Rev. B* **75**, 214419 (2007).
- [49] P. R. Stone, L. Dreher, J. W. Beeman, K. M. Yu, M. S. Brandt, and O. D. Dubon, Interplay of epitaxial strain and perpendicular magnetic anisotropy in insulating ferromagnetic  $\text{Ga}_{1-x}\text{Mn}_x\text{P}_{1-y}\text{N}_y$ , *Phys. Rev. B* **81**, 205210 (2010).
- [50] P. Czarnik, J. Dziarmaga, and P. Corboz, Time evolution of an infinite projected entangled pair state: An efficient algorithm, *Phys. Rev. B* **99**, 035115 (2019).
- [51] A. Kshetrimayum, M. Rizzi, J. Eisert, and R. Orús, Tensor network annealing algorithm for two-dimensional thermal states, *Phys. Rev. Lett.* **122**, 070502 (2019).
- [52] J. Gubernatis, N. Kawashima, and P. Werner, *Quantum Monte Carlo Methods: Algorithms for Lattice Models* (Cambridge University Press, 2016).
- [53] F. Becca and S. Sorella, *Quantum Monte Carlo Approaches for Correlated Systems* (Cambridge University Press, 2017).
- [54] W. M. C. Foulkes, L. Mitas, R. J. Needs, and G. Rajagopal, Quantum Monte Carlo simulations of solids, *Rev. Mod. Phys.* **73**, 33 (2001).
- [55] T. Senthil, A. Vishwanath, L. Balents, S. Sachdev, and M. P. A. Fisher, Deconfined Quantum Critical Points, *Science* **303**, 1490 (2004).
- [56] H. Shao, W. Guo, and A. W. Sandvik, Quantum criticality with two length scales, *Science* **352**, 213 (2016).
- [57] J. Takahashi and A. W. Sandvik, Valence-bond solids, vestigial order, and emergent  $\text{SO}(5)$  symmetry in a two-dimensional quantum magnet, *Phys. Rev. Research* **2**, 033459 (2020).
- [58] B. Zhao, J. Takahashi, and A. W. Sandvik, Multicritical Deconfined Quantum Criticality and Lifshitz Point of a Helical Valence-Bond Phase, *Phys. Rev. Lett.* **125**, 257204 (2020).
- [59] Z. H. Liu, M. Vojta, F. F. Assaad, and L. Janssen, Metallic and Deconfined Quantum Criticality in Dirac Systems, *Phys. Rev. Lett.* **128**, 087201 (2022).
- [60] E. Y. Loh, J. E. Gubernatis, R. T. Scalettar, S. R. White, D. J. Scalapino, and R. L. Sugar, Sign problem in the numerical simulation of many-electron systems, *Phys. Rev. B* **41**, 9301 (1990).
- [61] N. Kawashima and K. Harada, Recent Developments of World-Line Monte Carlo Methods, *J. Phys. Soc. Jpn.* **73**, 1379 (2004).
- [62] T. Nishino and K. Okunishi, Corner Transfer Matrix Renormalization Group Method, *J. Phys. Soc. Jpn.* **65**, 891 (1996).
- [63] R. Orús and G. Vidal, Simulation of two-dimensional quantum systems on an infinite lattice revisited: Corner transfer matrix for tensor contraction, *Phys. Rev. B* **80**, 094403 (2009).
- [64] P. Corboz, T. M. Rice, and M. Troyer, Competing States in the  $t$ - $J$  Model: Uniform  $d$ -Wave State versus Stripe State, *Phys. Rev. Lett.* **113**, 046402 (2014).
- [65] H. C. Jiang, Z. Y. Weng, and T. Xiang, Accurate Determination of Tensor Network State of Quantum Lattice Models in Two Dimensions, *Phys. Rev. Lett.* **101**, 090603 (2008).
- [66] H. N. Phien, J. A. Bengua, H. D. Tuan, P. Corboz, and R. Orús, Infinite projected entangled pair states algorithm improved: Fast full update and gauge fixing, *Phys. Rev. B* **92**, 035142 (2015).
- [67] P. Corboz, Variational optimization with infinite projected entangled-pair states, *Phys. Rev. B* **94**, 035133 (2016).
- [68] L. Vanderstraeten, J. Haegeman, P. Corboz, and F. Verstraete, Gradient methods for variational optimization of projected entangled-pair states, *Phys. Rev. B* **94**, 155123 (2016).
- [69] H.-J. Liao, J.-G. Liu, L. Wang, and T. Xiang, Differentiable Programming Tensor Networks, *Phys. Rev. X* **9**, 031041 (2019).
- [70] Y.-H. Chen, K. Hsu, W.-L. Tu, H.-Y. Lee, and Y.-J. Kao, Variational tensor network operator, arXiv:2207.01819 10.48550/arXiv.2207.01819 (2022).
- [71] W.-L. Tu, E.-G. Moon, K.-W. Lee, W. E. Pickett, and H.-Y. Lee, Field-induced Bose-Einstein condensation and supersolid in the two-dimensional Kondo necklace, *Commun. Phys.* **5**, 130 (2022).
- [72] J. Hasik, G. B. Mbeng, W.-L. Tu, and S.-S. Diop, A tensor network library for two-dimensional lattice models, <https://github.com/jurajHasik/peps-torch> (2020).
- [73] W.-Y. Liu, J. Hasik, S.-S. Gong, D. Poilblanc, W.-Q. Chen, and Z.-C. Gu, The emergence of gapless quantum spin liquid from deconfined quantum critical point, arXiv:2110.11138 10.48550/arXiv.2110.11138 (2021).
- [74] J. Hasik, M. V. Damme, D. Poilblanc, and L. Vanderstraeten, Simulating chiral spin liquids with projected entangled-pair states, arXiv:2201.07758 10.48550/arXiv.2201.07758 (2022).
- [75] H.-K. Wu and W.-L. Tu, Competing quantum phases of hard-core bosons with tilted dipole-dipole interaction, *Phys. Rev. A* **102**, 053306 (2020).
- [76] S. Singh, R. N. C. Pfeifer, and G. Vidal, Tensor network states and algorithms in the presence of a global  $\text{U}(1)$  symmetry, *Phys. Rev. B* **83**, 115125 (2011).
- [77] B. Bauer, P. Corboz, R. Orús, and M. Troyer, Implementing global abelian symmetries in projected entangled-pair state algorithms, *Phys. Rev. B* **83**, 125106 (2011).
- [78] P. Corboz, P. Czarnik, G. Kapteijns, and L. Tagliacozzo, Finite Correlation Length Scaling with Infinite Projected Entangled-Pair States, *Phys. Rev. X* **8**, 031031 (2018).
- [79] M. Rader and A. M. Läuchli, Finite Correlation Length Scaling in Lorentz-Invariant Gapless iPEPS Wave Functions, *Phys. Rev. X* **8**, 031030 (2018).
- [80] M. M. Rams, P. Czarnik, and L. Cincio, Precise Extrapolation of the Correlation Function Asymptotics in Uniform Tensor Network States with Application to the Bose-Hubbard and XXZ Models, *Phys. Rev. X* **8**, 041033 (2018).
- [81] A. Pelissetto and E. Vicari, Critical phenomena and renormalization-group theory, *Physics Reports* **368**, 549 (2002).
- [82] A. Aharony, O. Entin-Wohlman, and A. Kudlis, Different critical behaviors in perovskites with a structural phase transition from cubic-to-trigonal and cubic-to-tetragonal symmetry, *Phys. Rev. B* **105**, 104101 (2022).
- [83] A. Aharony, *Phase Transitions and Critical Phenomena*, edited by C. Domb and M. S. Green, Vol. 6 (Academic Press, New York, 1976) pp. 357–424.
- [84] P. M. Chaikin and T. C. Lubensky, *Principles of Condensed Matter Physics* (Cambridge University Press, 2012).
- [85] M. Kardar, *Statistical Physics of Fields* (Cambridge University Press, 2012).
- [86] J. Cardy, *Scaling and Renormalization in Statistical Physics* (Cambridge University Press, 2015).